

PROCEEDINGS OF SPIE

SPIDigitalLibrary.org/conference-proceedings-of-spie

Pattern recognition based strategy to evaluate the stress field from dynamic photoelasticity experiments

Briñez-de León, Juan C., Rico-G., Mateo, Branch, John, Restrepo-M., Alejandro

Juan C. Briñez-de León, Mateo Rico-G., John W. Branch, Alejandro Restrepo-M., "Pattern recognition based strategy to evaluate the stress field from dynamic photoelasticity experiments," Proc. SPIE 11509, Optics and Photonics for Information Processing XIV, 115090I (21 August 2020); doi: 10.1117/12.2568630

SPIE.

Event: SPIE Optical Engineering + Applications, 2020, Online Only

Pattern recognition-based strategy to evaluate the stress field from dynamic photoelasticity experiments

Juan C. Briñez-de León^{*a,b,c}, Mateo Rico-G.^a, John W. Branch^b, Alejandro Restrepo-M.^{b,c},

^a Institución Universitaria Pascual Bravo, Facultad de Ingeniería, Departamento de Ingeniería Electrónica. Grupo GIIAM, Medellín, Colombia.

^b Universidad Nacional de Colombia- Sede Medellín- Facultad de Minas. Departamento de Ciencias de la Computación. Grupo GIDIA, Medellín, Colombia.

^c Universidad Nacional de Colombia- Sede Medellín- Facultad de Minas. Departamento de Ingeniería Mecánica. Grupo GPIMA- Núcleo el Río, Bloque 04. Carrera 64C No. 63 – 120, Medellín, Código Postal 050034- Colombia.

ABSTRACT

For avoiding fails in loaded structures, adjust their geometry, removing material, or quantify residual stresses, photoelasticity studies often is limited by complex experiments, excessive computational procedures, expert supervision, narrow applications, and static focus. This paper proposes a pattern recognition-based strategy for evaluating the stress field from simplex dynamic experiments. Here, temporal color variations are processed to extract, select and classify stress magnitudes, isotropic points, and inconsistent information. This approach used synthetic photoelasticity videos from analytical stress models about disk and ring under diametric compression. Additional to improve limitations in conventional photoelasticity approaches, this strategy identifies isotropic and inconsistent points.

Keywords: Digital photoelasticity, stress evaluation, pattern recognition, temporal color analysis.

1. INTRODUCTION

Patterns recognition-based strategies have allowed many engineering areas to identify key information in complex phenomena that are difficult to represent with single math functions [1]. This implies that making computational descriptions about a specific phenomenon can be useful to identify patterns in it, and consequently relate them to specific behaviors. Between the physical phenomena attended by pattern recognition strategies, time dependent applications have been highlighted by the powerful contributions that a feature-based representation introduce when understanding a phenomenon, overall for such scenarios in which the spatial information is not enough to anticipate a resultant effect [2].

In relation to time-dependent applications, dynamic photoelasticity is an optical technique used experimentally to evaluate the mechanical response experienced by bodies subjected to load conditions [3]. In this field of study, literature reports that principal drawbacks come from the fact that mechanical information is wrapped by color fringe patterns that not only change spatially with the body geometry and the optical arrangement for making visual the phenomenon, but also with every load condition applied during the dynamic process [4]. This has made the scientist community stablish as priority to achieve the stress evaluation in full field by using single experiments and computational procedures, which could be extended to industrial applications.

With the intention of responding to the photoelasticity needs, recent methods in literature have converged to the importance of evaluating the stress field from strategies that use one single optical configuration when observing the dynamic phenomenon [5]. This with the intention of saving time when recording the fringe patterns, and avoiding errors introduced when manipulating the optical elements. And, although different proposals have been developed in such direction, there still exist limitations such as specialized optical configurations [6], color calibration dependence [7], regularized optimization methods [8], lost information in critical zones [9], inconsistency detections [10], identification of isotropic points for material removal [11], among others.

In response to conventional limitations in photoelasticity studies, recent works have explored the relationships between spatial stress conditions and temporal color changes [12]. There, it was introduced the possibility of recognizing stress categories from temporal color behaviors acquired under a fixed polariscope configuration [13]. However, the photoelasticity problem was only addressed by considering four stress categories into a discrete representation of the stress field [14], which opened a challenge toward improving the representation and classifications of color dynamics in order to evaluate the stress information beyond such stress categories, and be able to identify isotropic points and inconsistency zones introduced by the principal stress directions.

Taking advantages of the previous works in dynamic photoelasticity, and also in the research opportunities in terms of improving the stress evaluation in critical stress zones, isotropic points and inconsistency regions, this paper proposes a pattern recognition-based strategy to evaluate the stress field under a single polariscope configuration. In this case, dynamic photoelasticity cases are represented as digital image sequences. There, every pixel position into the sequence produces a color trajectory, which is posteriorly described through a collection of features and classified by using an artificial neural network (ANN). The importance of this method lies in the fact that color trajectories, in such manner, are threatened individually while ignoring its spatial connections with other pixel positions. Therefore, the stress evaluation process became invariant to the body geometry.

Next sections present a theoretical framework about dynamic cases in digital photoelasticity, and a classical approximation to pattern recognition-based approaches. Likewise, methods and procedures will be described, and finally results and conclusions.

2. THEORETICAL FRAMEWORK

As an overview of this paper, the proposed approach looks for describing the color trajectories generated in dynamic photoelasticity experiments by using features capable to discriminate between different stress information such as stress magnitudes, inconsistency zones, and isotropic points. To achieve this objective, this section starts by introducing the concepts around the color trajectories generated from dynamic photoelasticity experiments. After that, the section also introduces the classical operation mode for pattern recognitions approaches.

2.1 Dynamic photoelasticity

Digital photoelasticity is an experimental technique to visualize and quantify the stress information distributed into a loaded body [3]. In this field of study, conventional methods are referred to experiments in which the applied load is considered as static. Thus, dynamic cases are often treated as a sequence of static conditions [4]. In those cases, the stress visualization is due to the use of materials which become birefringent when stressed ' $n_1 - n_2 = C(\sigma_1 - \sigma_2)$ '. This implies that the principal stress difference ' $\sigma_1 - \sigma_2$ ' induces a phase delay (δ) in the light traveling through the loaded body, as indicates in (1) by the stress optic law.

$$\delta = \frac{2\pi h C(\sigma_1 - \sigma_2)}{\lambda} \quad (1)$$

In addition to the need of birefringent materials, digital photoelasticity requires specialized optical assemblies, called as polariscopes, for making visual the stress information, as illustrated in by the Figure 1 for a circular polariscope. In that case, the stress map is wrapped into a digital image with color fringe patterns. There, the intensities are a function of the spectral content of light source ' $I_b(\lambda)$ ', rotations of the optical elements, principal stress difference ' $\sigma_1 - \sigma_2$ ', stress direction ' θ ', and the spectral response of camera sensor ' $S_{R,G,B}(\lambda)$ ', as indicated in (2) where the first polarizer is rotated as ' $\rho = \pi/2$ ', and first quarter wave plate as ' $\gamma = \pi/4$ '. There, ' φ ' and ' β ' represent the rotations for the second quarter wave plate and second linear polarizer, respectively.

$$I_{R,G,B} = \frac{1}{\lambda_2 - \lambda_1} \sum_{\lambda_1}^{\lambda_2} \left(I_b(\lambda) * \sin 2(\beta - \varphi) \cos(\delta) - \sin(\theta - \varphi) \cos(\beta - \varphi) \sin(\delta) * S_{R,G,B}(\lambda) \right) \quad (2)$$

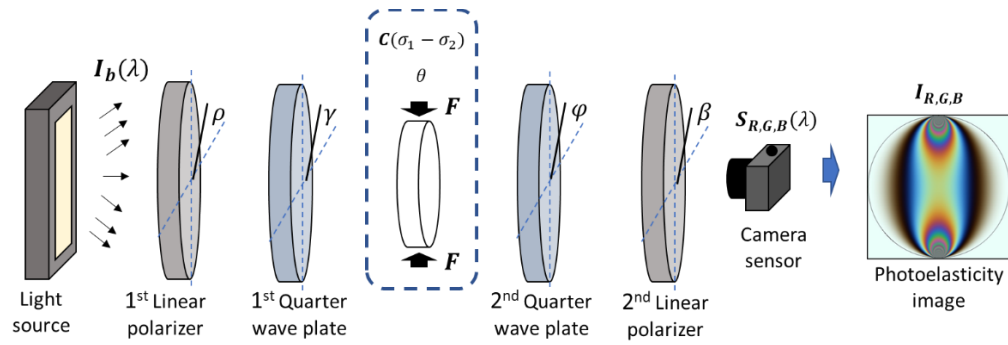


Figure 1. Representation of a circular polariscope assembled around a compressed disk. Element rotations as ' $\rho = \pi/2$ ', ' $\gamma = \pi/4$ ', ' $\varphi = -\pi/4$ ' and ' $\beta = \pi/2$ '.

For dynamic experiments, the applied load ' F ' is a time-dependent function ' $F(t)$ ', and therefore, the output in the process is a sequence of photoelasticity images in which the color fringe patterns vary depending of the load curve. In this case, the loads change incrementally [5]. It implies that fringe densities get increased frame by frame with the load augmentation, as shown in the Figure 2 for a disk with six load increments.

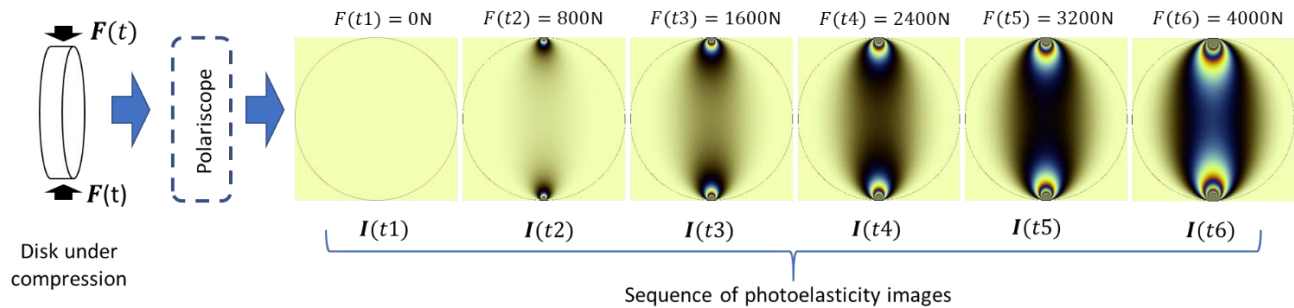


Figure 2. Effect of dynamic loads inn a disk under compression. In the polariscope: fluorescent light source, bright field configuration, and DCC3260 camera sensor.

Beyond of perceiving the dynamic photoelasticity experiments as a set of static conditions in which the stress evaluation is carried out in a sampled way, new dynamic tendencies assume the sequences of photoelasticity images as an array of temporal color evolutions according to every pixel position. In this paper, such color variations are so-called as color trajectories. This implies that every point into the resultant stress field within a loaded body is associated to one specific color trajectory extracted from the same position into the image sequence, as illustrated by the Figure 3 for a point with high stress into a compressed disk.

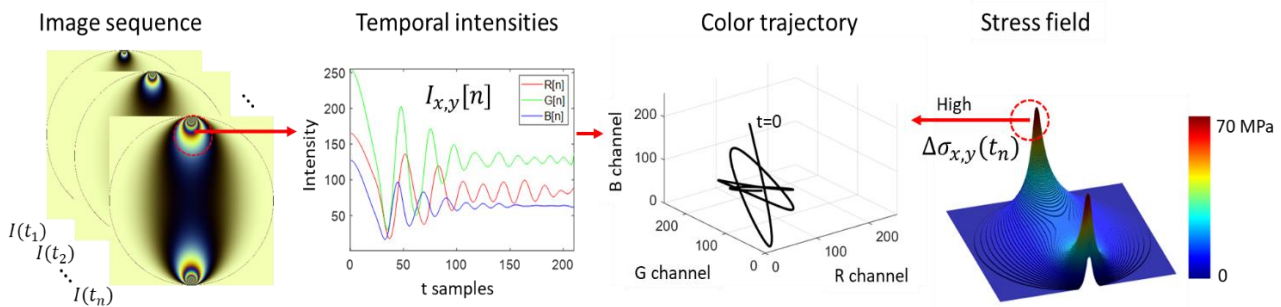


Figure 3. Color trajectory and its relationship with the stress field for a case of stress concentration in a disk under compression.

2.2 Pattern recognition-based approaches

Pattern recognition-based approaches attempt for identifying patterns and regularities within data collections [1]. They are used in many of the engineering areas by their capability of representing the phenomena through feature vectors, which can be separable into a n-dimensional space by using classifiers. Pattern recognition strategies have different steps such as data structure, preprocessing, feature extraction and feature selection, and finally to implement a classification method, as illustrated in the Figure 4 for a conventional scheme about pattern recognition-based approach.

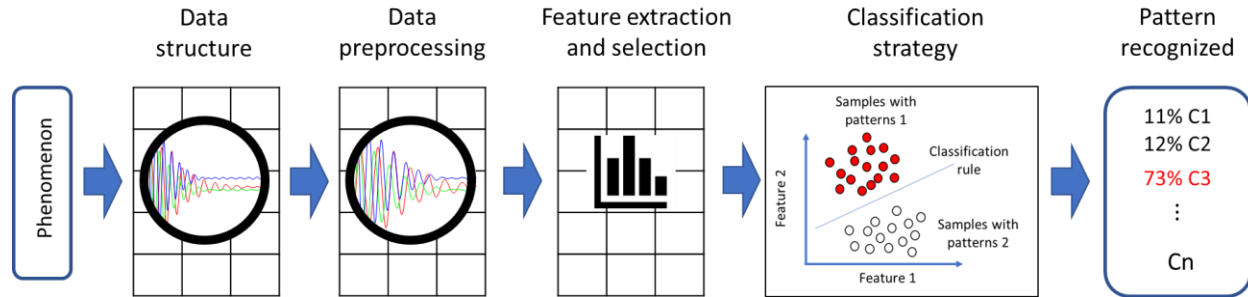


Figure 4. Scheme for a conventional pattern recognition-based strategy.

There exist different operational modes in classification strategies. However, supervised methods are highlighted because have enough samples of the phenomena and its respective effects expressed as labels [2]. In those cases, every sample is represented as feature vector by using descriptors, which depend on the data nature. In those cases, the classifiers are chosen depending on the complexity in which the feature vectors can be differentiated according to the labels. In the case of complex classifications, artificial neural networks are often implemented because they skirt the problem of programming the separation rule by learning it from the data collection.

3. METHODS AND PROCEDURES

In principle, the proposed approach starts with the data generation because the absence of public photoelasticity repositories. With this step, a labeling process is performed to remark the continue stress surface into categorical stress problem. After that, different types of color trajectories are analyzed in order to understand the behaviors which define a stress category. Finally, the proposed pattern recognition strategy is presented.

3.1 Data generation

From a systemic point of view, photoelasticity experiments require as inputs the stressed body, the light source, rotations of the elements into the polariscope, and a camera sensor [15]. This means that simulating every one of such parts, synthetic experiments can be carried out, as illustrated in the Figure 5. In the cases of stressed bodies, this paper uses the analytic models of the benchmark geometries reported in literature such as disk and ring under compression, as presented in the Table 1 for the geometry configurations. There, loads are applied in '210' steps without exceeding the elastic limit for the 'pmma' material. Stress optical coefficient is ' $C=4.5 \times 10^{-12} \text{N/m}^2$ '.

Table 1. Experimental parameters of the loaded bodies.

Geometry	Ratios	Load range	Thickness
Disk	$R_{\text{ext}}=25\text{mm}$	From 0 to 3500N	10mm
Ring_1	$R_{\text{ext}}=25\text{mm}$, $R_{\text{int}}=2.5\text{mm}$	From 0 to 3200N	10mm
Ring_2	$R_{\text{ext}}=25\text{mm}$, $R_{\text{int}}=5\text{mm}$	From 0 to 3000N	10mm
Ring_3	$R_{\text{ext}}=25\text{mm}$, $R_{\text{int}}=10\text{mm}$	From 0 to 3000N	10mm

With respect to the light source and camera sensor, this paper considered the spectral content of a white led, and spectral response of the DCC 3260 sensor, respectively. Finally, for the circular polariscope configuration, element rotations that produce bright field images, and two type of inconsistencies were considered, as summarized in Table 2. With these experimental configurations, '12' sequences of images with 210 frames, every one, were generated. Spatial images resolutions were 850x850 pixels.

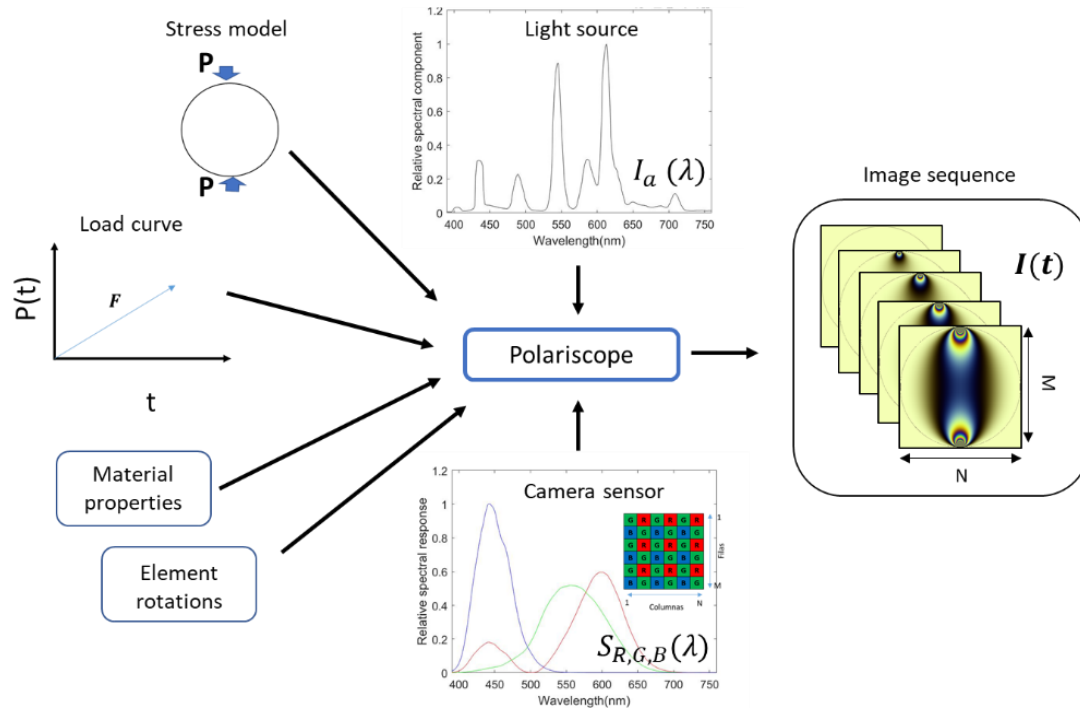


Figure 5. Scheme of the generation of a synthetic experiment given a specific material, a polariscope configuration, the spectral content of a light source, and the spectral response of a camera sensor.

Table 2. Polariscope configurations for generating the synthetic photoelasticity experiments. Configurations according to Patterson and Wang 1991 [23].

Type	Element rotations				Intensity equation
	ρ	γ	φ	β	
Bright field	90°	45°	-45°	90°	$I1 = \frac{1}{\lambda_2 - \lambda_1} \sum_{\lambda=\lambda_1}^{\lambda_2} 0.5I_b(\lambda)[1 + \cos(\delta(\lambda))]S_{R,G,B}(\lambda)$
Inconsistency 1	90°	45°	90°	0°	$I3 = \frac{1}{\lambda_2 - \lambda_1} \sum_{\lambda=\lambda_1}^{\lambda_2} 0.5I_b(\lambda)[1 - \sin(\delta(\lambda))\sin(2\theta)]S_{R,G,B}(\lambda)$
Inconsistency 2	90°	45°	-45°	45°	$I4 = \frac{1}{\lambda_2 - \lambda_1} \sum_{\lambda=\lambda_1}^{\lambda_2} 0.5I_b(\lambda)[1 + \sin(\delta(\lambda))\cos(2\theta)]S_{R,G,B}(\lambda)$

3.2 Data labeling

Currently, the stress field is evaluated as a continuous surface. However, to remark the evaluation into a pattern recognition-based strategy, this work develops a discretization process in which different stress ranges were converted into stress labels according to the maximum stress allowed. In this case, five stress labels were generated from the stress surface such as: critical with stresses upper 80% of elastic limit, high with stresses between 40% and 80%, medium between 10% and 40%, low with stresses between 1% and 10%, and isotropic points with stresses lower than 1%. In addition to the labels for stress magnitudes, the inconsistencies induced by the principal stress direction were joined into an inconsistency stress label. In summary, a stress map was generated per every polariscope configuration, as summarized in the Table 3 for disk and rings under compression.

Table 3. Label stress maps for different polariscope configurations and different stressed geometries.

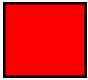
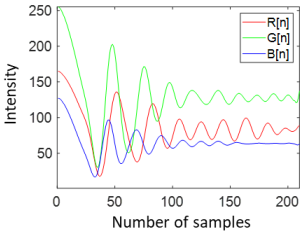

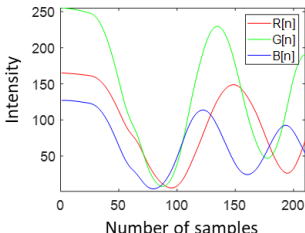
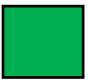
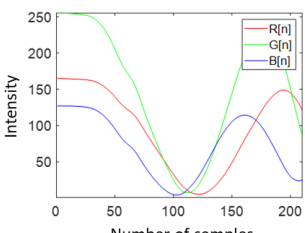

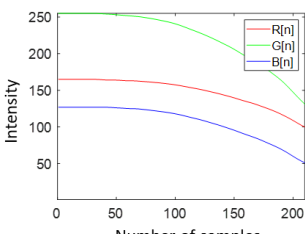

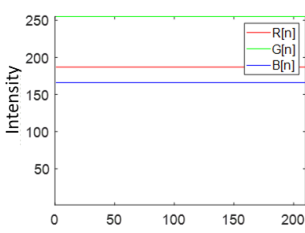

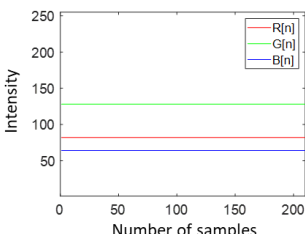
Geometry	Label map for bright field	Label map for inconsistency 1	Label map for inconsistency 2	Labels												
Disk				<table><tr><td>1</td><td>Critical</td></tr><tr><td>2</td><td>High</td></tr><tr><td>3</td><td>Med</td></tr><tr><td>4</td><td>Low</td></tr><tr><td>5</td><td>Isotropic</td></tr><tr><td>6</td><td>inconsistence</td></tr></table>	1	Critical	2	High	3	Med	4	Low	5	Isotropic	6	inconsistence
1	Critical															
2	High															
3	Med															
4	Low															
5	Isotropic															
6	inconsistence															
Ring 1																
Ring 2																
Ring 3																

3.3 Relationship between color trajectories and stress labels

Every pixel position into a sequence of photoelasticity images corresponds with a stress label within the label map. This implies that each color trajectory can be analyzed with respect to one stress category. For this stage, the Table 4 describes the general dynamic in the color trajectory per stress category. In the first case, the critical stress categories show color dynamics with strong oscillations that tend to converge in one specific color value. Similarly, high, medium, and low stress categories show color oscillations but with less temporal changes.

In a general approximation, the dynamic differences in color trajectories are mainly described by the number of crests and peaks into the color evolution. Where, low stress category develops the least number of oscillations. In the case of isotropics points, color trajectories do not experience temporal changes. There, color intensities tend to maintain the background intensities. In a similar condition, stress category with inconsistencies are characterized by being constant through the time. In this case, the offset color value is a type of gray by the polariscope element rotations which conduce to isoclinic fringes.

Table 4. Description of color trajectories per stress categories.

Stress label	Color trajectory	Main description
Critical 		<p>More than six observable color oscillations, RGB color components tend to be attenuated through the time.</p>
High 		<p>Around three observable color oscillations, blue color component is more attenuated than red and green color.</p>
Medium 		<p>Around two crests within the color oscillations, blue color component is more attenuated than red and green color.</p>
Low 		<p>Less than one crest within the color oscillations, blue color component experiences lower intensities than red and green color components.</p>
Isotropic 		<p>Non oscillations. Constant behavior through the time.</p>
Inconsistency 		<p>Non oscillations. Constant behavior through the time.</p>

3.4 Data structure and preprocessing

In order to describe the color trajectories through feature vectors, this stage takes samples from every sequence of color images. In this case, a quarter of the trajectories per sequence were chosen, as it is indicated in the Figure 6. There, an array of 185250 trajectories was generated. Likewise, a data vector with stress labels was generated according to the sampling process applied to color trajectories. After that, a subsampling process was applied to obtain a balanced dataset with 29490 samples, 4915 color trajectories per stress categories. In the Figure, 'T' array contains the temporal color information per color trajectory in the RGB color space. Complementarily, the 'd' vector containing the stress labels stored for matching with the color trajectory positions.

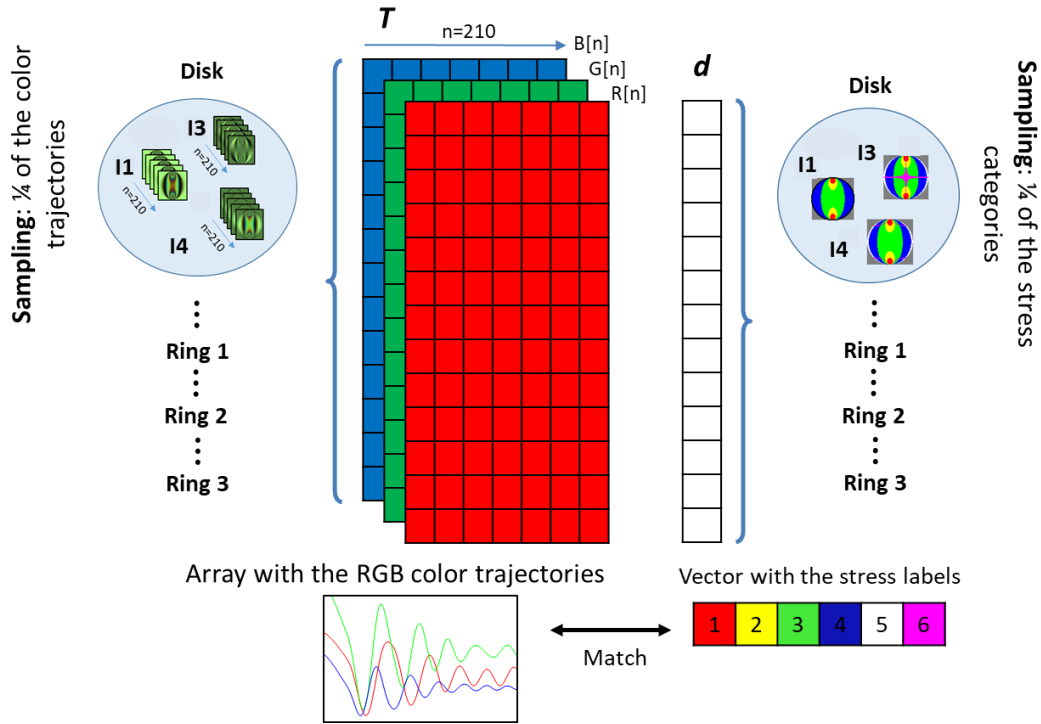


Figure 6. Scheme for structuring the data about color trajectories and stress categories.

Posterior to the data subsampling process, this paper includes a preprocessing stage to reduce the noise into the color trajectories. For this, a smooth filter was included. In this case, the filter was applied to every color component by averaging every sampled data with respect to a neighborhood of 15 samples, as expressed in (3). This parameter was tuned experimentally to avoid intensity reductions into the color temporal evolution. Where $T_2R_k(i)$ is the 'R' component of the color trajectory in a 'k' position into the data array, 'i' and 'j' account for the time samples. The unknown 'M' is the number of neighbors into the temporal average operation [16].

$$T_2R_k(i) = \begin{cases} \frac{1}{M} \sum_{j=0}^{M-1} T_R_k(i-j), & \text{if } i > (M-1) \\ \frac{1}{i} \sum_{j=0}^{i-1} T_R_k(i-j), & \text{to the rest} \end{cases} \quad (3)$$

3.5 Feature extraction and selection

Quantifying the attributes for representing the dynamics of temporal color trajectories is a task directly related to the nature photoelasticity phenomenon. In this case, the temporal color variations are processed channel by channel considering the integration of different descriptors such as time, frequency and 1D-LBP, as summarized in the Table 5 for the R color component, green and blue color components can be represented similarly. From this process, a concatenated data vector ' X_k ' is generated per color trajectory. Our descriptors are based on features according to the analysis of color trajectories

presented previously, which express differences among stress labels. These descriptors attempt for distinguishing between static color evolutions as experienced in isotropic and inconsistency points.

Table 5. Feature descriptors for photoelasticity color trajectories.

Type	Name	Feature expression	Number of features	Reference
Time	RMS value	$RMS_{R_k} = \frac{1}{\#Frames} \sqrt{\sum_{b=1}^{\#Frames} (T_{2R_k}(b))^2}$	1 per channel	[17]
	Kurtosis	$K_{R_3} = \frac{\sum_{b=1}^{\#Frames} (T_{2R_k}(b) - \overline{T_{2R_k}})^4}{RMS_{R_k}^4}$	1 per channel	[17]
	Crest factor	$CRF_{R_k} = \frac{Peak(T_{2R_k})}{RMS_{R_k}}$	1 per channel	[18]
	Crossing the mean	$CN_{R_k} = \sum_{b=1}^{\#Frames} \{if, T_{2R_k}(b) = \overline{T_{2R_k}}\}$	1 per channel	[17]
	Slope changes	$SN_{R_k} = \sum_{b=1}^{\#Frames} \{if, \begin{aligned} &sign(T_{2R_k}(b+1) - T_{2R_k}(b)) \\ &\neq sign(T_{2R_k}(b) - T_{2R_k}(b-1)) \end{aligned}\}$	1 per channel	[18]
	Impulse factor	$IMF_{R_k} = \frac{Peak(T_{2R_k})}{\frac{1}{\#Frames} \sum_{b=1}^{\#Frames} T_{2R_k}(b) }$	1 per channel	[17]
	Standard deviation	$SD_{R_k} = \frac{1}{\#Frames} \sqrt{\sum_{b=1}^{\#Frames} (T_{2R_k}(b) - \overline{T_{2R_k}})^2}$	1 per channel	[17]
Frequency	Spectral magnitude	$MFFT_{R_k} = \sqrt{[R(fft(T_{2R_k}))]^2 + [i(fft(T_{2R_k}))]^2}$	105 per channel	[13]
	Power spectral density	$PSD_{R_k} = \frac{1}{\#f} \sum_{b=1}^{\#f} fft(T_{2R_k}(b)) ^2$	1 per channel	[18]
	Peak intensity	$FPI_{R_k} = \max(fft(T_{2R_k}) ^2)$	1 per channel	[18]
	Spectral centroid	$SC_{R_k} = \frac{\sum_{b=1}^{\#f} ffft(T_{2R_k}(b)) * fft(T_{2R_k}(b)) ^2}{\sum_{b=1}^{\#f} fft(T_{2R_k}(b)) ^2}$	1 per channel	[17]
Texture	LBP-1D	$HLBP_{R_k} = \text{Hist}(LBP_{R_k})$	59 per channel	[14]
Total	Concatenation	$X_{R_k} = Time + Frequency + Texture$	174 per channel	N.A

From all the description strategies a feature vector of 522 data length was generated to represent the dynamic of the color trajectories. With this, a Rank-based strategy for feature selection was carried out to reduce the vector length [19]. In this

case, ‘12’ features were chosen per every descriptor type. With this stage, it was noted that best ranked features were such related to the number of oscillations in to the color trajectories such as: the number of slope changes in the time descriptors, first frequencies of the spectral content of the fast Fourier transform, and classes with the number of crest and increment directions into the LBP histogram. Likewise, features for temporal standard deviation were selected.

3.6 Classification

From previous stages, an array ‘X’ with 36 features and 29490 instances was generated. Likewise, a label vector ‘d’ about six stress categories was defined. With them, an artificial neural network was trained as classifier having into account 80% samples per training (23592) and 20% for testing (5898). In this case, the network parameters are reported in the Table 6 having into account the multilayer perceptron architecture [20].

Table 6. Parameters of the artificial neural network used as classifier.

Parameter	Configuration
Input neurons	36
Hidden layers	10
Output neurons	6
Activation function	Hyperbolic tang.
Cost function	Cross entropy.
Optimizer	Gradient descent.
Learning rate	0.3
Training epochs	1000
Performance metric	Global accuracy and performance per stress category according to the confusion matrix.

3.7 Validation strategy

Beyond to obtain the stress category given a color trajectory, this section emphasizes on the quality in which the classification strategy is capable to evaluate the complete stress field into a dynamic situation. Thus, the stress categories are initially recognized from the color trajectories in all the pixel positions. After that, the complete recovered map is compared with the categorical stress maps established as reference when generating the analytical models, as illustrated in the Figure 7 for the disk under diametric compression. In these cases, comparison metrics are the mean squared error ‘MSE’ and the Structural Similarity Index, as proposed in [21].

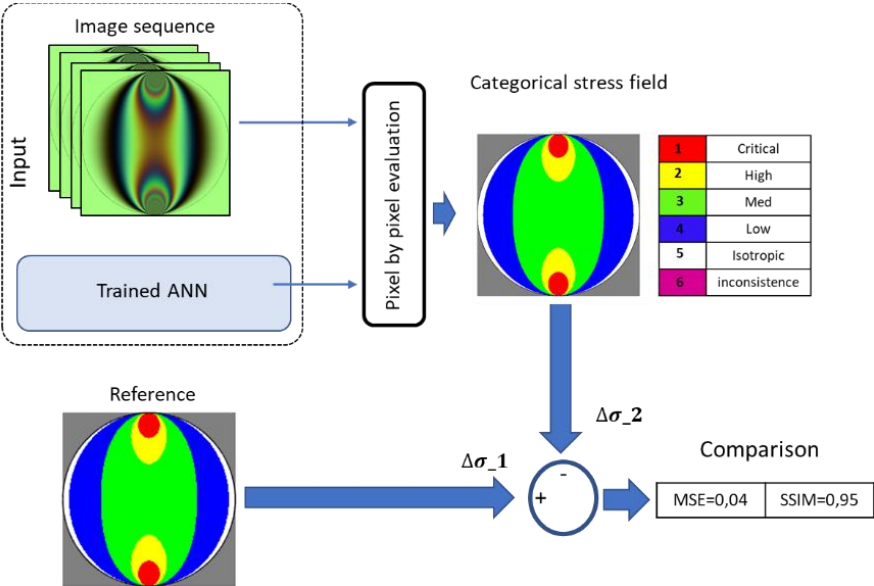


Figure 7, Scheme for approach validation. Case: disk under diametric compression.

4. RESULTS AND ANALYSIS

Although many procedures have been mentioned into the classification strategy, this section only shows the result under the perspective of the classifier as recognizer of stress categories from color trajectories, and its performance when evaluating the whole stress field.

4.1 Classification performance

In the case of the training curve, the error decrements show that the proposed network achieves the best discrimination performance with 163 epochs, as presented in the Figure 8a by using the Matlab®, specifically the Artificial Neural Networks Toolbox [22]. In that case, training error decreased lower than 0.01.

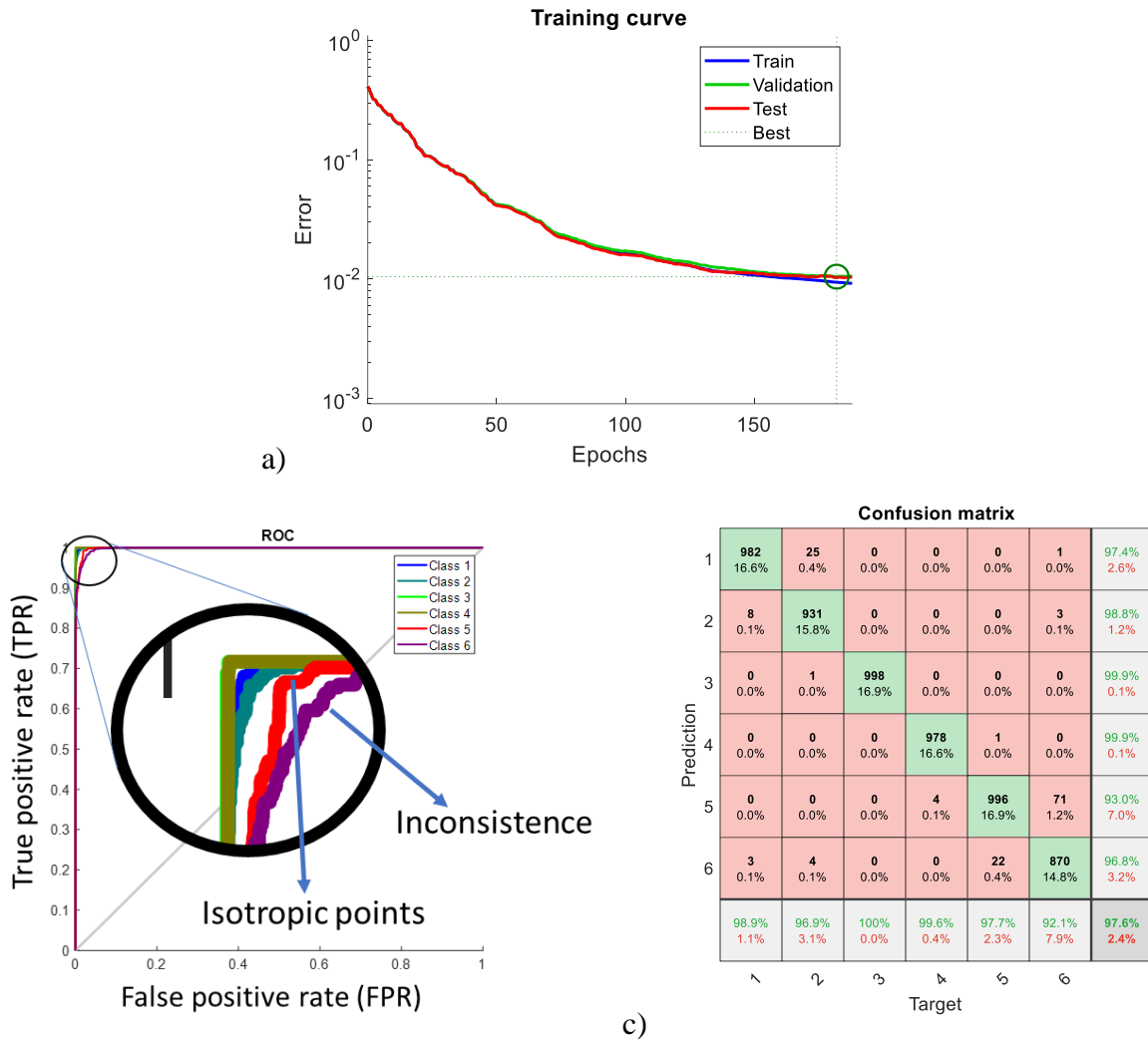


Figure 8. Classification results. a) Training curve, b) ROC curve, and c) confusion matrix.

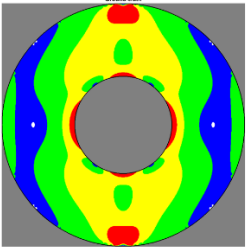
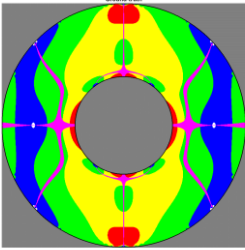
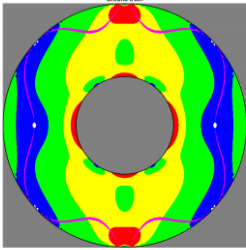
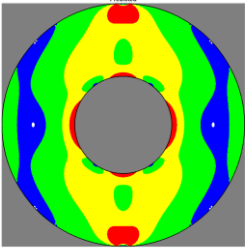
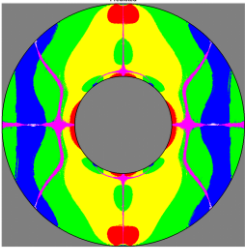
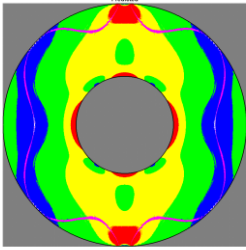
Although all the stress categories show high performance into the ROC curve, the class 5 and class 6 experience lower performance. Those are the classes for isotropic and inconsistency points, indicating that categorical stress levels are better represented per the color trajectories than such dynamics with static color evolutions, as can be verified into the confusion matrix. There, the global performance shows a classification value around '97.6%'. The class 1, which correspond to the critical stress achieved a classification performance over '98.9%'. Color trajectories for high stress values were classified with 96.9% performance. The medium stress category was the best classified with '100%' performance. Low stress

category, and isotropics points were classified with a performance of ‘99.6%’ and ‘97.7%’, respectively. Finally, color trajectories for inconsistency point were the worst classified with a performance about with ‘92.1%’. These results indicate that, in general, dynamics in color trajectories contain information that can be useful to differentiate between stress categories. However, isotropics points must be better described.

4.2 Stress field evaluation

With respect to the classification process for all the pixel positions within an image sequence, the Table 7 shows the results for the Ring_3 under diametric compression. In that case, the first row presents the analytical reference maps, called as ‘Target’ in this section. Second row shows the predicted stress maps, and finally, the comparison metrics of ‘MSE’ and ‘SSIM’ are presented in the last two rows, respectively. These results also include the comparison per type of polariscope configuration according to the bright field, inconsistency 1 and inconsistency 2.

Table 7. Classification performance when evaluating the stress field in a disk under diametric compression by considering three type of polariscope configurations.

	Bright field	Inconsistency 1	Inconsistency 2
Target			
Predicted			
MSE	0.05	0.09	0.06
SSIM	0.92	0.90	0.92

Categorical recovered stress maps for the Ring_3 under diametric compression presented high similarity with respect to the reference analytic maps, even, for sequence of images that were acquired under polariscope configurations which introduce inconsistencies. In these cases, the SSIM values performances that are over 90%, generally. The worst performance sequences of images with inconsistencies, which could be attributed to the difficulty to represent the color trajectories in such points. From these results, it could be inferred that differences between the type of inconsistencies are due to the size of the inconsistency regions per polariscope configuration.

In concordance with the previous ring geometry, the remaining experimental configurations performed similarly, as summarized in the Table 8 through the ‘MSE’ and ‘SSIM’ metrics according to the three polariscope configurations and the four analyzed geometries. In this case, the best result was obtained for the disk under diametric compression when observing it through a bright field polariscope configuration, as highlighted with red color. The worst stress evaluation performance was achieved for inconsistency 1, which match with presented result per the complete ring geometry. With these results, differences among the body geometries could be attributed to the quantity of color trajectories in every

sequence of images, and the temporal color attenuation effect that the spectral interaction between the light source and camera sensor introduce into the color trajectories.

Table 8. Performance evaluation of the stress field by using the classification strategy according to the integration of three polariscope configurations and four body geometries.

Experiments	Bright field		Inconsistency 1		Inconsistency 2	
	MSE	SSIM	MSE	SSIM	MSE	SSIM
Disk	0.04	0.95	0.15	0.84	0.09	0.88
Ring_1	0.11	0.91	0.22	0.82	0.15	0.87
Ring_2	0.04	0.94	0.10	0.91	0.06	0.93
Ring_3	0.05	0.92	0.09	0.90	0.06	0.92

5. CONCLUSIONS

A pattern recognition-based strategy was implemented to evaluate the stress field in loaded bodies. With this approach, the temporal information about the color behavior into photoelasticity image sequences was used to identify stress categories without dependence of the polariscope configuration. It implies that dynamics in color trajectories contain significant information for discriminating among stress conditions, including different experimental parameters.

The integration of different feature descriptors into the dynamic representation of color trajectories make easier the stress recognition process, overall for such cases in which the dynamic information can not be only described by the intensity oscillations as it is the case of isotropic and inconsistency points.

Although the classification process develops high performance in the principal stress categories, a punctual analysis suggest that isotropic and inconsistency points require a better representation. This approach could be useful to evaluate the stress field of loaded bodies in industrial cases where the applications are limited by the multiple polariscope configurations, or situations in which the acquisition assemblies conduce to images with inconsistencies.

REFERENCES

- [1] Bulgarevich, D. S., Tsukamoto, S., Kasuya, T., Demura, M., & Watanabe, M. (2018). Pattern recognition with machine learning on optical microscopy images of typical metallurgical microstructures. *Scientific reports*, 8(1), 1-8.
- [2] Mabrouk, A. B., & Zagrouba, E. (2017). Spatio-temporal feature using optical flow based distribution for violence detection. *Pattern Recognition Letters*, 92, 62-67.
- [3] Briñez-de León, J. C., Martínez, A. R., & Bedoya, J. W. B. (2016). High stress concentration analysis using RGB intensity changes in dynamic photoelasticity videos. In *2016 XXI Symposium on Signal Processing, Images and Artificial Vision (STSIVA)* (pp. 1-7). IEEE.
- [4] Xu, L. R., & Rosakis, A. J. (2003). An experimental study of impact-induced failure events in homogeneous layered materials using dynamic photoelasticity and high-speed photography. *Optics and Lasers in Engineering*, 40(4), 263-288.

- [5] Pandey, A., & Ramesh, K. (2019). Development of a New Normalization Technique for Twelve Fringe Photoelasticity (TFP). In *Advancement of Optical Methods & Digital Image Correlation in Experimental Mechanics, Volume 3* (pp. 177-180). Springer, Cham.
- [6] Diner, D. J., Davis, A., Hancock, B., Geier, S., Rheingans, B., Jovanovic, V., ... & McClain, S. C. (2010). First results from a dual photoelastic-modulator-based polarimetric camera. *Applied optics*, 49(15), 2929-2946.
- [7] Swain, D., Thomas, B. P., Philip, J., & Pillai, S. A. (2015). Novel calibration and color adaptation schemes in three-fringe RGB photoelasticity. *Optics and Lasers in Engineering*, 66, 320-329.
- [8] Quiroga, J. A., Servin, M., & Marroquin, J. L. (2001). Regularized phase tracking technique for demodulation of isochromatics from a single tricolour image. *Measurement Science and Technology*, 13(1), 132.
- [9] Briñez de León, J. C., Fandiño Toro, H. A., Branch Bedoya, J. W., & Restrepo Martínez, A. analysis of resolution on photoelasticity images: dynamic load case. <http://hdl.handle.net/11349/21963>
- [10] Liu, X., & Dai, S. (2015). Mathematical morphology guided automatic unwrapping isoclinic phase map in white light photoelasticity. *Journal of the Optical Society of Korea*, 19(6), 643-648.
- [11] Surendra, K. V. N., & Simha, K. Y. (2015). Digital image analysis around isotropic points for photoelastic pattern recognition. *Optical Engineering*, 54(8), 081209.
- [12] Ju, Y., Ren, Z., Wang, L., Mao, L., & Chiang, F. P. (2018). Photoelastic method to quantitatively visualise the evolution of whole-field stress in 3D printed models subject to continuous loading processes. *Optics and Lasers in Engineering*, 100, 248-258.
- [13] Briñez de León, J. C., Martínez, A. R., & Bedoya, J. W. B. (2019, June). Fast Fourier Transform as Color Variation Descriptor for Imaging the Stress Field from Photoelasticity Videos. In *Imaging Systems and Applications* (pp. JW2A-46). Optical Society of America.
- [14] Briñez de León, J. C., Mery, D., Restrepo, A., & Branch, J. W. (2019, September). One-dimensional local binary pattern based color descriptor to classify stress values from photoelasticity videos. In *Optics and Photonics for Information Processing XIII* (Vol. 11136, p. 1113607). International Society for Optics and Photonics.
- [15] Briñez-de León, J. C., Restrepo-Martínez, A., & Branch-Bedoya, J. W. (2019). Computational analysis of Bayer colour filter arrays and demosaicking algorithms in digital photoelasticity. *Optics and Lasers in Engineering*, 122, 195-208.
- [16] Liu, Y., Liu, C., & Wang, D. (2009). A 1D time-varying median filter for seismic random, spike-like noise elimination. *Geophysics*, 74(1), V17-V24.
- [17] Sejdić, E., Lowry, K. A., Bellanca, J., Redfern, M. S., & Brach, J. S. (2013). A comprehensive assessment of gait accelerometry signals in time, frequency and time-frequency domains. *IEEE Transactions on Neural Systems and Rehabilitation Engineering*, 22(3), 603-612.

- [18] Sapsanis, C., Georgoulas, G., & Tzes, A. (2013, June). *EMG based classification of basic hand movements based on time-frequency features*. In *21st Mediterranean Conference on Control and Automation* (pp. 716-722). IEEE.
- [19] Chandrashekar, G., & Sahin, F. (2014). *A survey on feature selection methods*. *Computers & Electrical Engineering*, 40(1), 16-28.
- [20] Restrepo-Martinez, A., & Briñez, J. C. (2019, September). *Dynamic color descriptor based Frenet-Serret to classify stress zones from pixel variations recorded in photoelasticity videos*. In *Optics and Photonics for Information Processing XIII* (Vol. 11136, p. 111360G). International Society for Optics and Photonics.
- [21] Sara, U., Akter, M., & Uddin, M. S. (2019). *Image quality assessment through FSIM, SSIM, MSE and PSNR—a comparative study*. *Journal of Computer and Communications*, 7(3), 8-18.
- [22] Arulmozhi, V. (2011). *Classification task by using Matlab Neural Network Tool Box—A Beginner's View*. *International Journal of Wisdom Based Computing*, 1(2), 59-60.
- [23] Patterson, E. A., & Wang, Z. (1991). *Advantages and disadvantages in the application of phase stepping in photoelasticity*. *Applied solid mechanics*, 4, 358.